



ARL-TR-7282 • MAY 2015



US Army Research Laboratory

Low VHF Channel Measurements and Simulations in Indoor and Outdoor Scenarios

by Fikadu T Dagefu, Gunjan Verma, Chirag R Rao, Paul L Yu, Jonathan R Fink, Brian M Sadler, and Kamal Sarabandi

NOTICES

Disclaimers

The findings in this report are not to be construed as an official Department of the Army position unless so designated by other authorized documents.

Citation of manufacturer's or trade names does not constitute an official endorsement or approval of the use thereof.

Destroy this report when it is no longer needed. Do not return it to the originator.



Low VHF Channel Measurements and Simulations in Indoor and Outdoor Scenarios

by Fikadu T Dagefu, Gunjan Verma, Chirag R Rao, Paul L Yu, Jonathan R Fink, Brian M Sadler, and Kamal Sarabandi
Computational & Information Sciences Directorate, ARL

Kamal Sarabandi
Department of Electrical Engineering and Computer Science, University of Michigan

| REPORT DOCUMENTATION PAGE | | | | Form Approved OMB No. 0704-0188 | |
|--|-----------------------------|------------------------------|--|--|---|
| <p>Public reporting burden for this collection of information is estimated to average 1 hour per response, including the time for reviewing instructions, searching existing data sources, gathering and maintaining the data needed, and completing and reviewing the collection information. Send comments regarding this burden estimate or any other aspect of this collection of information, including suggestions for reducing the burden, to Department of Defense, Washington Headquarters Services, Directorate for Information Operations and Reports (0704-0188), 1215 Jefferson Davis Highway, Suite 1204, Arlington, VA 22202-4302. Respondents should be aware that notwithstanding any other provision of law, no person shall be subject to any penalty for failing to comply with a collection of information if it does not display a currently valid OMB control number.</p> <p>PLEASE DO NOT RETURN YOUR FORM TO THE ABOVE ADDRESS.</p> | | | | | |
| 1. REPORT DATE (DD-MM-YYYY) May 2015 | | 2. REPORT TYPE Final | | 3. DATES COVERED (From - To) October 2014-April 2015 | |
| 4. TITLE AND SUBTITLE Low VHF Channel Measurements and Simulations in Indoor and Outdoor Scenarios | | | | 5a. CONTRACT NUMBER | |
| | | | | 5b. GRANT NUMBER | |
| | | | | 5c. PROGRAM ELEMENT NUMBER | |
| 6. AUTHOR(S) Fikadu T Dagefu, Gunjan Verma, Chirag R Rao, Paul L Yu, Jonathan R Fink, Brian M Sadler, and Kamal Sarabandi | | | | 5d. PROJECT NUMBER | |
| | | | | 5e. TASK NUMBER | |
| | | | | 5f. WORK UNIT NUMBER | |
| 7. PERFORMING ORGANIZATION NAME(S) AND ADDRESS(ES) US Army Research Laboratory ATTN: RDRL-CIN-T Adelphi, MD 20783-1138 | | | | 8. PERFORMING ORGANIZATION REPORT NUMBER ARL-TR-7282 | |
| 9. SPONSORING/MONITORING AGENCY NAME(S) AND ADDRESS(ES) | | | | 10. SPONSOR/MONITOR'S ACRONYM(S) | |
| | | | | 11. SPONSOR/MONITOR'S REPORT NUMBER(S) | |
| 12. DISTRIBUTION/AVAILABILITY STATEMENT Approved for public release; distribution is unlimited. | | | | | |
| 13. SUPPLEMENTARY NOTES primary author's email: <fikadu.t.dagefu.ctr@mail.mil>. | | | | | |
| 14. ABSTRACT The lower VHF band has potential for low power, short-range communications, as well as for geolocation applications, in both indoor and urban environments. Most prior work at low VHF focuses on longer range path loss modeling. In this report, we study indoor/outdoor near-ground scenarios through experiments and electromagnetic wave propagation simulations for both line-of-sight (LOS) and non-LOS (NLOS) cases, at ranges up to 200 meters. Mounting our receiver on a robotic platform enabled the collection of thousands of measurements over an extended indoor/outdoor test area. We measure the channel transfer function with pulse and tone probe signals. Based on statistical tests, we show that the measured channels have a nearly ideal scalar attenuation and delay transfer function, with minimal phase distortion. Compared with higher VHF and above, the measured short-range VHF channels do not exhibit small-scale fading, which simplifies communications receiver signal processing, and enables phase and amplitude based geolocation techniques. | | | | | |
| 15. SUBJECT TERMS Channel characterization, Lower VHF band, propagation measurements, miniaturized antennas, transfer function measurements | | | | | |
| 16. SECURITY CLASSIFICATION OF: | | | 17. LIMITATION OF ABSTRACT UU | 18. NUMBER OF PAGES 48 | 19a. NAME OF RESPONSIBLE PERSON Fikadu T Dagefu |
| a. REPORT Unclassified | b. ABSTRACT Unclassified | c. THIS PAGE Unclassified | | | 19b. TELEPHONE NUMBER (Include area code) 301-394-0405 |

Contents

| | |
|--|------------|
| List of Figures | v |
| List of Tables | vi |
| Acknowledgments | vii |
| 1. Introduction | 1 |
| 2. Multipath Analysis and Full-Wave Simulation | 3 |
| 3. Measurement System | 6 |
| 3.1 System Hardware | 6 |
| 3.1.1 Radio and Daughtercards | 6 |
| 3.1.2 Antenna | 7 |
| 3.1.3 Mobile Robotic Collection Platform | 7 |
| 3.2 Data Acquisition Software | 9 |
| 4. Measurements and Processing | 10 |
| 4.1 Measurement Scenarios | 10 |
| 4.2 Pulse Tests | 13 |
| 4.2.1 Pulse Test Parameters | 13 |
| 4.2.2 Wider Bandwidth Pulse Tests | 16 |
| 4.3 Tone Tests | 16 |
| 4.4 Bit Error Rate (BER) Measurements | 16 |
| 5. Experimental Results | 17 |
| 5.1 Path Loss | 17 |
| 5.2 Phase Distortion and Instantaneous Phase | 19 |
| 5.3 Statistical Analysis of the Measured Channel Transfer Function | 20 |
| 5.4 Tone Tests for Transfer Function Phase Measurement | 24 |
| 5.5 BER Measurement Results | 26 |
| 6. Conclusion | 28 |

| | |
|---|-----------|
| 7. References | 30 |
| List of Symbols, Abbreviations, and Acronyms | 36 |
| Distribution List | 38 |

List of Figures

| | | |
|---------|---|----|
| Fig. 1 | The FDTD simulation geometry used for phase distortion analysis | 4 |
| Fig. 2 | Phase variation of the received signal as a function of frequency | 6 |
| Fig. 3 | Measurement system diagram | 7 |
| Fig. 4 | Simulated S11 and radiation pattern of the $\lambda/6$ antenna | 8 |
| Fig. 5 | The USRP integrated on a PackBot mobile platform | 9 |
| Fig. 6 | Measurement Scenario 1 | 11 |
| Fig. 7 | Measurement Scenario 2 | 12 |
| Fig. 8 | Measurement Scenario 3 | 12 |
| Fig. 9 | The root-raised cosine waveform used in our pulse tests | 13 |
| Fig. 10 | Mean and standard deviation of measured path-loss | 19 |
| Fig. 11 | Instantaneous phase versus time of received pulses | 20 |
| Fig. 12 | Mean square deviation of the received signal phase: cases 5a & 5b | 21 |
| Fig. 13 | Mean square deviation of the received signal amplitude: cases 5a & 5b | 21 |
| Fig. 14 | Mean square deviation of the measured phase: case 3d | 22 |
| Fig. 15 | Tone tests: Case 2a, at Rx point P3 | 25 |
| Fig. 16 | Tone tests: Case 2a, at Rx point P4 | 25 |
| Fig. 17 | Tone tests: Case 2a, at Rx point P5 | 26 |
| Fig. 18 | Theoretical and measured BER vs SNR curves: LoS case | 27 |
| Fig. 19 | Theoretical and measured BER vs SNR curves: NLOS case | 27 |

List of Tables

| | | |
|---------|---|----|
| Table 1 | Measurement scenarios and Tx/Rx locations | 10 |
| Table 2 | Parameters used for measurements | 10 |

Acknowledgments

We would like to thank Jeffrey N Twigg, Jason M Gregory, Dr Ethan Stamp, Dr John Rodgers, and Stuart H Young of the US Army Research Laboratory for their support with the robotic integration and experiments. We would also like to thank Mr Jihun Choi of the University of Michigan for help with the fabrication of the antennas used in this work.

INTENTIONALLY LEFT BLANK.

1. Introduction

Reliable wireless communication is of paramount importance for many important civilian and military applications. In scenarios where the propagation environment is challenging, such as in complex terrain, urban canyons, and indoor environments, achieving a reliable communications link that is not significantly impeded by the presence of obstacles and scatterers is extremely challenging. In recent years, rapid global urbanization and the ever-increasing need for reliable communications in emergency and tactical applications^{1,2} has necessitated reliable communications paradigms for such challenging environments. Networks are needed to support humans and autonomous agents, incorporating communications, sensing, real-time positioning, and tracking.^{3,4}

State-of-the-art communications systems that operate in the upper very high frequency (VHF) through microwave bands suffer from significant attenuation and small-scale fading, as well as phase distortion caused by high levels of multipath.⁵⁻⁷ In a complex environment at these frequencies, without line of sight (LOS), multipath propagation is the dominant signal source between a transmitter and a receiver, whereas the direct path signal is often extremely weak due to penetration loss. Major effort has been devoted over many decades to design sophisticated multipath mitigation techniques, incorporating channel coding and modulation schemes to overcome the challenges introduced by the channel.⁸⁻¹³ Such schemes add significantly to transceiver hardware and software complexity, still may only provide marginal performance in challenging scenarios, e.g., necessitating networking over many hops or a high transmit power.

The lower VHF band has significant potential to support low complexity, low power, highly reliable communications. This primarily stems from the fact that in the lower VHF scatterers are small in terms of wavelength.^{3,14} Consequently, strong penetration through multiple walls and buildings can be achieved at relatively low power. Reflection, scattering, and diffraction phenomena are dramatically reduced, thereby greatly minimizing multipath fading, yielding a short-range channel that is LOS-like in terms of very slight phase distortion and delay spread. This liberates the system designer at low VHF from the typically stringent requirements on power, system bandwidth, and complex equalization processing needed in ultra-high frequency (UHF) and microwave based systems.

Of course, conventional antennas such as dipoles operating in the lower VHF band are very large, limiting application of such systems to stationary cases or large platforms. In the case of mobile nodes with smaller antennas, the transmit power must be high enough to compensate for the poor efficiency of the antennas. Thus far, the large size of conventional antennas has been a major obstacle in terms of their large-scale deployment in mobile scenarios within highly cluttered environments. However, due to recent advances in antenna miniaturization techniques and the development of palm-sized lower VHF antennas with good performance,^{15,16} interest in low power, low data rate communications in this band is increasing. Thus, there is a need to better understand the channel characteristics in this band, so as to better inform and guide the design of systems operating at the lower VHF band.

While the frequency allocations vary in different regions of the world, in North America, there is dual allocation at low VHF, consisting of primary and secondary allocations. For example, the primary allocation near 38 and 40 MHz is for Federal use, including research and development and test range operations. Other applications and users include the industrial, scientific, and medical (ISM) band, the US Army's Single Channel Ground and Airborne Radio System (SINCGARS), highway patrol radios, and ocean radars.^{17,18}

The large majority of channel characterization in complex propagation scenarios has consisted of path loss measurements in support of long-range commercial wireless applications, which operate in the upper UHF and microwave range.^{19–24} These studies typically assume a powerful base station with an elevated antenna serving mobile units located near-ground,¹ as is common in cellular phone and other mobile communications. In contrast, little attention has been paid to shorter-range lower VHF band channel characterization for near-ground nodes deployed in complex propagation scenarios, especially for indoor-to-indoor and outdoor-to-indoor communications. Urban path-loss models in the upper VHF and military UHF bands based on field measurements have been presented.^{1,25} Similar path-loss models in the lower VHF range have also been proposed.^{2,26–33} However, classical empirically derived urban propagation models, often geared toward conventional cellular applications, in which a base station is situated at a relatively high elevation, are not appropriate for near-ground nodes and such models are not necessarily valid at the lower VHF and high frequency (HF) bands.^{31,32} Here we primarily focus on measuring the channel transfer function and phase distortion in the lower VHF; extensive path-loss measurements have been reported,³³ including experimental comparison

of path loss at 40 MHz and 2.4 GHz for indoor and indoor/outdoor cases.

Simulation-based propagation models have also been proposed to understand channel characteristics of multipath scenarios in VHF/UHF bands.^{34–36} In previous studies,^{37–40} investigations of short-range HF/VHF propagation in forested environments have been presented. There has also been some effort in developing systems operating in the HF band for near-field communication and geolocation applications.^{41,42} We note that the majority of research regarding propagation and channel modeling in the HF/VHF band is concerned with long-range ionospheric propagation.^{43,44}

In this report, we study near-ground, wireless channel modeling in the lower VHF band for indoor and indoor/outdoor scenarios, drawing from extensive propagation measurements and simulations using a finite-difference time-domain (FDTD) based electromagnetic model. In Section 2, the full-wave electromagnetic simulation results are described. In Section 3, our 40-MHz measurement system is discussed, including our software-defined radio (SDR) transmit and receive tools, as well as integration onto a robotic platform for ease of data collection over large areas. In Sections 4 and 5, we present the measurement scenarios, experimental results, and analysis based on our measurements, including path loss, small-scale fading, phase distortion, and bit error rate (BER) measurements.

2. Multipath Analysis and Full-Wave Simulation

In this section, we consider the multipath channel and associated channel transfer function. This is a precursor to measuring and estimating the channel transfer function in amplitude and phase. An indoor/outdoor propagation simulation is used as an initial look at the problem (later we consider a physical scene that is very similar to the simulation). These results set the stage for our experiments in the sections that follow, including statistical tests for the presence or absence of multipath, testing for an ideal transfer function, and communications BER performance without equalization.

Our simulation geometry is shown in Fig. 1. In the upper UHF to microwave bands, ray tracing approaches are often used to simulate wave propagation. Ray tracing is relatively straightforward and computationally tractable under the assumption that the size of the scatterers in the environment is generally much larger than the wavelength. However, this assumption breaks down in the lower VHF, where the

size of some scatterers becomes comparable to the wavelength. For this reason, we resort to a technique that directly solves Maxwell's equations to characterize the wireless channel in the lower VHF band. In particular, we use EMCUBE, a commercial full-wave solver based on FDTD.⁴⁵

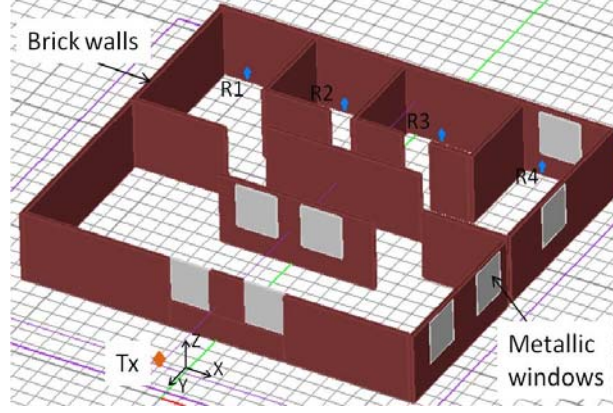


Fig. 1 The FDTD simulation geometry used for short-range phase distortion analysis. The walls are modelled as homogeneous dielectric slabs and metal sheets are introduced to simulate the propagation characteristics of windows.

The simulation scene in Fig. 1 consists of several walls, floor, and ceiling, as well as doors and windows (the floor and ceiling are not shown in the figure for clarity). The floor is modeled as a half-space homogeneous dielectric medium with a dielectric constant of concrete ($\epsilon_r = 4.5 + j0.011$). The walls are modeled as dielectric slabs with a dielectric constant of brick ($\epsilon_r = 4 + j0.001$). To make this indoor scenario more realistic, rectangular metal sheets (1.2 m by 1.2 m) are included to simulate the effect of windows as shown in the figure. The dimensions of the overall scenario are 15 m by 15 m by 3.3 m. The geometry is kept relatively small in order to make the simulation more computationally tractable. A vertically polarized dipole antenna positioned outdoors is used as a transmitter (Tx), emitting a Gaussian envelop pulse that is frequency translated to 40 MHz, with a 1-MHz bandwidth. Four vertically polarized receive (Rx) antennas are positioned indoors and the received signal from each antenna is recorded. Note that the Rx positions are symmetrically positioned on either side of the Tx antenna along the x axis.

In addition to path loss, we consider the phase coherence and memory in the channel. Denote the linear time invariant channel impulse response as

$$h(n) = \sum_{k=0}^{N-1} P_k e^{j\phi_k} \delta(n - n_k), \quad (1)$$

where P_k and ϕ_k are the amplitude and phase of the k^{th} component of the signal. The $k = 0$ term corresponds to the first arrival in time, where we assume $n_0 < n_1 < \dots < n_{N-1}$ model the delays of the N multipath components. Taking the Fourier transform, we can express the transfer function as

$$H(f) = P_0 e^{j\phi_0} e^{-j2\pi f n_0} + \sum_{k=1}^{N-1} P_k e^{j\phi_k} e^{-j2\pi f n_k}, \quad (2)$$

where P_k and ϕ_k are the amplitude and phase of the k^{th} component of the Fourier transform of $h(n)$. The transfer function phase can be written as

$$\angle H(f) = \tan^{-1} \left[\frac{P \sin(\phi_0 - 2\pi f n_0) + \sum_{k=1}^{N-1} P_k \sin(\phi_k - 2\pi f n_k)}{P \cos(\phi_0 - 2\pi f n_0) + \sum_{k=1}^{N-1} P_k \cos(\phi_k - 2\pi f n_k)} \right]. \quad (3)$$

Generally, in the presence of multipath, the transfer function phase in Eq. 3 is a nonlinear function of frequency. If the amplitude of secondary multipath components is small, the first term in Eq. 2 will be the dominant component. In that case, all terms $k \geq 1$ in Eq. 2 can be ignored, and only the leading term in the numerator and denominator of Eq. 3 will be significant, resulting in a phase that is linear in frequency given by $\phi - 2\pi f n_0$. In Fig. 2, the phase of the received signal at each receive antenna position is plotted against frequency, centered around 40 MHz. The linear phase variation (aside from phase wrapping) in the bandwidth of interest is evidence of the minimal effect of multipath in this scenario. Similar results (not shown) occur in the transfer function amplitude, which is flat across the simulated bandwidth. Although there is attenuation due to penetration, there is little to no evidence of multipath propagation or fading. For example, in the case of receiver position R_2 , there are 4 layers of walls between the transmit antenna, which is outside the building and the receiver located indoors. The received signal is predominantly

the component that penetrates through the walls along the shortest path between the Tx and Rx antennas. Reflections and multiple scattering between walls are very small due to the small size of the walls (note that the thickness of a typical wall is a small fraction of the wavelength at 40 MHz). If there was significant multipath, the phase variation would be nonlinear, which is not the case, as can be seen in Fig. 2.

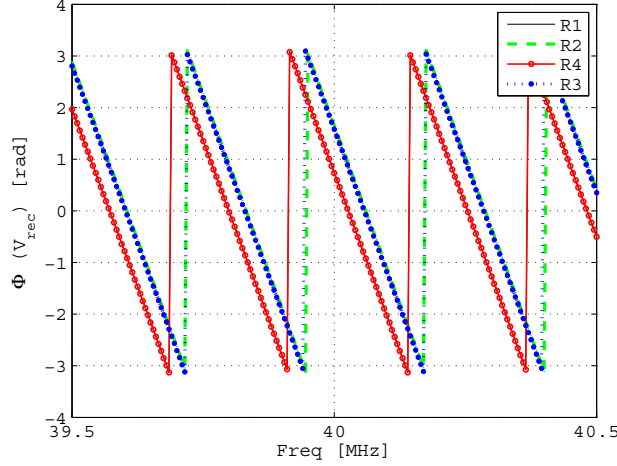


Fig. 2 Phase variation of the received signal as a function of frequency for the 4 Rx positions R_1 to R_4 as shown in Fig. 1, computed via an FDTD full-wave electromagnetic simulation of the scene.

3. Measurement System

In this section, we describe the hardware, peripherals, and software that we use to experimentally collect and analyze data. Figure 3 illustrates the 2 measurement systems employed. The 2 systems are essentially identical, except that in Fig. 3b we incorporate a reference channel by simultaneously transmitting the signal via the antenna and via cable to the receiver, enabling waveform distortion comparison, whereas in Fig. 3a the signal is only received via an antenna.

3.1 System Hardware

3.1.1 Radio and Daughtercards

We use the USRP model N210 SDR for our tests.⁴⁶ The USRP N210 provides an Ethernet interface that allows us to use software control for transmission and reception. The USRP is comprised of 2 parts: a motherboard consisting of an field-programmable gate array (FPGA), analog-to-digital convertor (ADC), and digital-to-analog convertor (DAC), and a modular daughtercard whose functions vary by

model, but may include filtering and up- and down-frequency conversion. The USRP N210 has a 100 MS/s ADC and 400 MS/s DAC. We use the BasicTx and BasicRx daughtercards at the transmitter and receiver, respectively, that provide access to signals in the 1 to 250 MHz range. These daughtercards do not have local oscillators or up/down conversion capability; we carry out these operations in the software. In our tests, we use 2 USRPs, one a dedicated transmitter and the other a dedicated receiver.

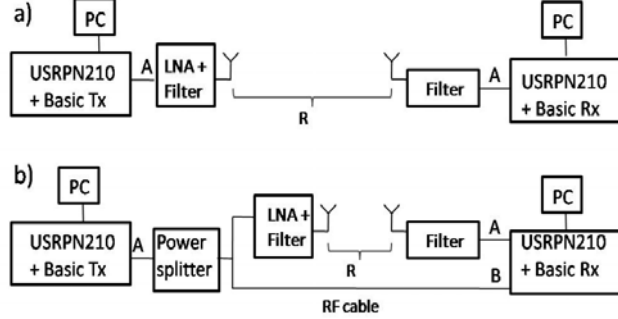


Fig. 3 USRP based, 1-way (dual channel) measurement system diagrams for a) pulse and packet tests, and b) tone tests. The pulse and packet tests are used to characterize the channel phase distortion and BER, respectively. For the tone test, a reference channel is introduced by cable connection, allowing direct comparison of the wireless and wired signals.

3.1.2 Antenna

The antenna used for these experiments is a $\lambda/6$ short dipole whose center frequency is tuned to 40 MHz. Because short dipoles have high capacitive reactance, a pair of high-Q loading coils are inserted on both arms of the dipole to increase the reactance and hence cancel out the capacitive effect, resulting in better matching with the transmission line feeding the antenna. The antenna has a gain of -2 dBi and a fractional bandwidth of 0.075. The antenna was measured using the outdoor elevated antenna measurement technique by mounting the antennas on 40-ft fiberglass towers. Simulated S11 and radiation pattern of the antenna are shown in Fig. 4. While in this report we focus on channel measurement and characterization, evolving miniature antenna designs operating in the upper HF and lower VHF band, with dimensions of $\lambda/100$ and smaller, have significant potential, especially for short-range, low power applications.¹⁵

3.1.3 Mobile Robotic Collection Platform

To efficiently conduct large-scale experiments, we integrated our USRP receiver onto a robotic platform, enabling data collection over extended indoor/outdoor envi-

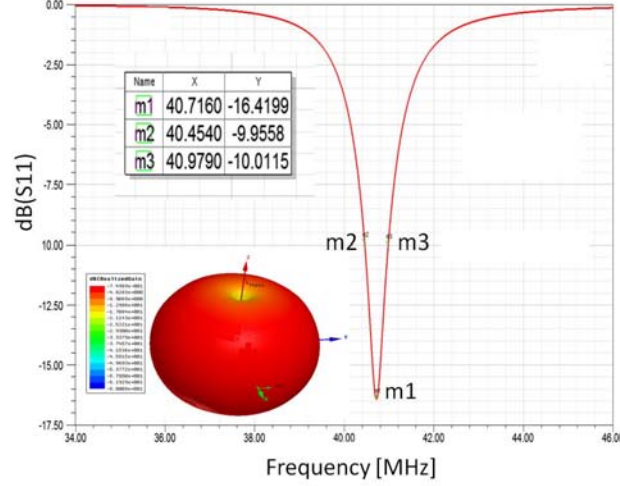


Fig. 4 Simulated S11 and radiation pattern of the $\lambda/6$ antenna used for all measurements. The center frequency was tuned to 40 MHz using the coils on the antenna.

ronments. The robot has the capability to carry out a simultaneous localization and mapping (SLAM) algorithm to provide a map and locate itself within the map. For our experiments, the robot is teleoperated throughout each scenario. By integrating the USRP with the robot control system, each radio measurement is automatically supplemented with time and position information. This enabled collection of large datasets over extended space and time (for example, see Scenario 3 in Section 4).

Referring to Fig. 5, we use the iRobot PackBot, outfitted with a Hokuyo UTM-30LX laser scanner, a pan-tilt unit, global positioning system (GPS), an onboard computer with Solid-state drive (SSD), and a Microstrain 3DM-GX2 inertial measurement unit (IMU); all of these instruments along with robot odometry data may be input to the SLAM algorithm for localization. The overall position error attributable to the system is about ± 1.5 m. To this baseline setup, we integrated a USRP N210 SDR, the $\lambda/6$ antenna, and a BB-2590 military battery cradle that supplies power to the SDR.

A Python script running on the onboard computer interfaces with the robot operating system (ROS), where the robot control and SLAM algorithms reside.^{46–49} This allows us to teleoperate the robot using an Xbox 360 wireless controller. When the robot stops, the Python script invokes a GNU radio function that captures a user-specified interval of data at a specified center frequency and sampling rate. The radio transmitter continuously emits the channel sounding signal of interest (tones

or pulses, depending on the particular experiment). The sampled radio data, as well as GPS, odometry, IMU, and laser scan data from the robot, are then recorded for later post-processing.

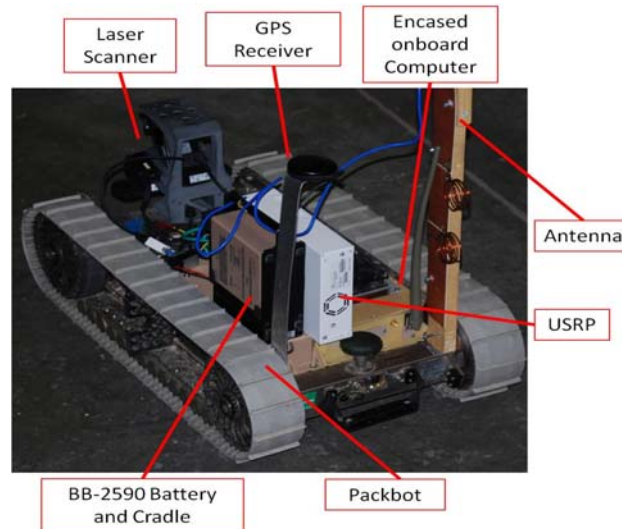


Fig. 5 The SDR receiver system integrated on a packbot mobile platform. Note the antenna is only partially visible.

3.2 Data Acquisition Software

We use signal processing software from the open-source GNU Radio project⁵⁰ and a custom MATLAB-USRP-Library (MUL)⁵¹ to control the USRPs and conduct our experiments. GNU Radio enables the implementation of SDR functions including filters, modulators, demodulators, channel coders, and many other elements.

For our tests, we suitably modify GNU Radio’s built-in code for our purposes; this code includes pure tone generation as well as complex baseband sample acquisition of the transmitted waveform. The MUL is a software-library that connects MATLAB to the USRP, allowing rapid conversion of communications-oriented MATLAB scripts into actual wireless experiments. We implemented a packetized communications link through MUL that allows for the generation and capture of packetized data that we use for the BER measurements described in Section 4.2.2.

4. Measurements and Processing

4.1 Measurement Scenarios

Measurements were carried out in 3 different environments, 2 indoor (Scenarios 1 and 2) and 1 extended indoor/outdoor (Scenario 3). Different cases are listed in Table 1, and experimental parameters are shown in Table 2. The Tx and Rx positions in Table 2 correspond to those marked in Figs. 6 through 8, as described next.

Table 1 Measurement scenarios indicating transmit locations and receiver regions, with reference to Figs. 6, 7, and 8, respectively. Most measurements consisted of NLOS propagation.

| | Environment | Tx position | Rx locations | Setup |
|---------|-------------|-------------|-------------------|-------|
| Case 1a | Scenario 1 | P_1 | $P_3 - P_6$ | NLOS |
| Case 1b | Scenario 1 | P_1 | $P_7 - P_{13}$ | NLOS |
| Case 1c | Scenario 1 | P_1 | P_3 | NLOS |
| Case 2a | Scenario 1 | P_2 | $P_3 - P_5$ | NLOS |
| Case 2b | Scenario 1 | P_0 | P_1 | LOS |
| Case 3a | Scenario 2 | P_1 | $P_2 - P_7$ | LOS |
| Case 3b | Scenario 2 | P_1 | $P_6 - P_7$ | LOS |
| Case 3c | Scenario 2 | P_1 | $P_7 - P_{11}$ | NLOS |
| Case 3d | Scenario 2 | P_1 | $P_8 - P_9$ | NLOS |
| Case 4 | Scenario 2 | P_0 | $P_{12} - P_{16}$ | NLOS |
| Case 5a | Scenario 3 | P_0 | R_0 | NLOS |
| Case 5b | Scenario 3 | P_1 | $R_4 - R_7$ | NLOS |
| Case 5c | Scenario 3 | P_0 | R_8, R_9 | NLOS |
| Case 5d | Scenario 3 | P_1 | $R_1 - R_3$ | NLOS |
| Case 5e | Scenario 3 | P_0 | R_8, R_9 | NLOS |

Table 2 Parameters used for measurements

| Parameter | Setting |
|-----------------|-----------------------------|
| Max. Tx power | 15 dBm (32 mW) |
| Tx,Rx Ant. Gain | -6.5 dBi, -6.5 dBi |
| Tx Ant. height | 1 m (0.13λ) |
| Rx Ant. height | 0.8 m, 1 m (0.1λ) |
| Tx, Rx pol. | V,V |
| Tx Amp. Gain | 40 dB |

Scenario 1 consists of indoor measurements in a multi-story, house-like test facility. Figure 6 shows a schematic of the first floor of this building, which has the same geometry as the one simulated (see Fig. 1 in Section 2). This is a wooden structure, including the floors, walls, and ceilings. As indicated in Fig. 6, steel cylinders and sheets were inserted as might occur in a home environment.

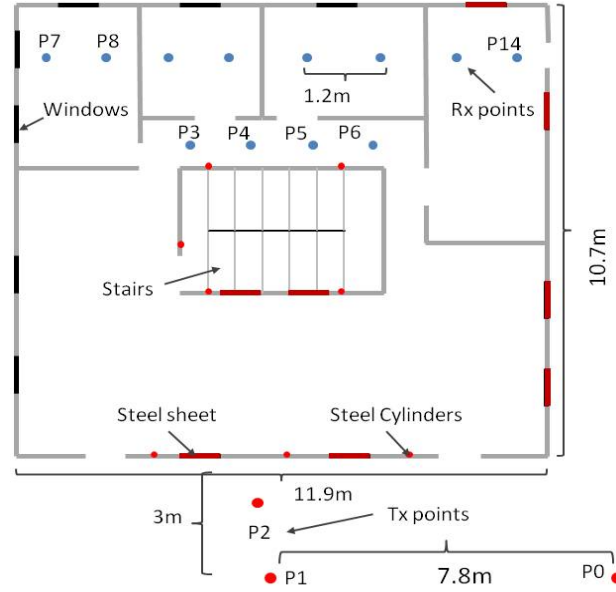


Fig. 6 Measurement Scenario 1: 2nd floor layout of wooden building, with steel sheets and cylinders introduced as shown

Scenario 2 is depicted in Fig. 7, interior to an office and laboratory building with extensive metal partitions, reinforced walls, and metal objects. Measurements were taken in the hallways, adjacent to offices and large interior lab bays. Measurements in Scenarios 1 and 2 were taken up to a maximum range of 40 m, in LOS and NLOS conditions.

For Scenario 3, the test facility shown in Fig. 8 was used, with a test diameter of about 200 m, consisting of multiple buildings constructed of concrete and cinderblock, with fences and other dielectric and metallic objects in the scene. Thousands of measurements were collected for the 2 different transmitter positions denoted P0 and P1 in the figure, teleoperating the mobile robotic collection platform within the denoted oval collection regions and along the dashed-line collection path shown.

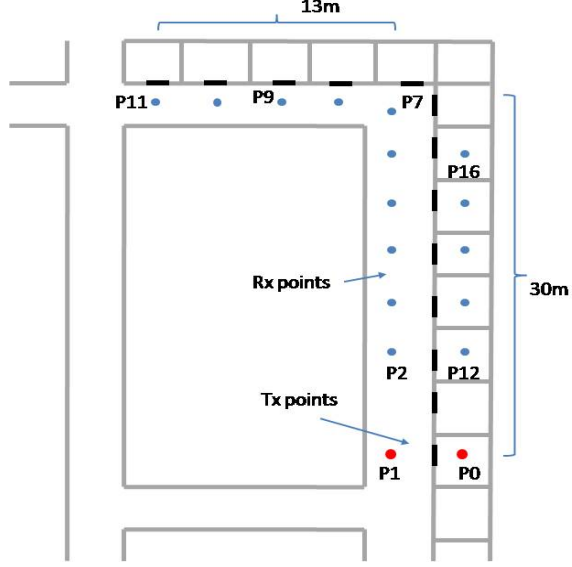


Fig. 7 Measurement Scenario 2: An L-shaped corridor in the 2nd floor of a much larger office and laboratory building with substantial metallic partitions and walls



Fig. 8 Measurement Scenario 3: overhead view of the test facility. P_0 and P_1 are the 2 transmitter positions and R_0 to R_9 are various indoor and outdoor regions traversed by the robot for data collection

4.2 Pulse Tests

In this section, we describe our pulse-based test for the presence of phase distortion (caused primarily by multipath propagation). These experiments are based on periodically transmitting root-raised cosine (RRC) pulses, a ubiquitous waveform used in digital communications.⁵²

4.2.1 Pulse Test Parameters

Let $p(n)$ denote the discrete-time RRC pulse. Figure 9 shows $p(n)$ and its corresponding analog waveform $p(t)$ after passing through the DAC. Referring to the RRC formula in Proakis,⁵² $p(t)$ has roll-off factor $\beta = 0.9$, symbol time $T_s = 3.2 \times 10^{-5}$ s, and pulse duration 1.28×10^{-4} s. We transmit a periodic pulse train with 8.72×10^{-4} s off-time between pulses during which null samples are fed to the DAC. Thus, the total time between 2 consecutive pulse starts is $T = 1.28 \times 10^{-4} + 8.72 \times 10^{-4} = 10^{-3}$ s. We transmit in both the in-phase (I) and quadrature (Q) channels, denoting the complex baseband equivalent as $p_c(t) = p(t) + jp(t)$. The RRC pulse has a 10 dB bandwidth of approximately 30 kHz, comfortably within the bandwidth of our antenna.

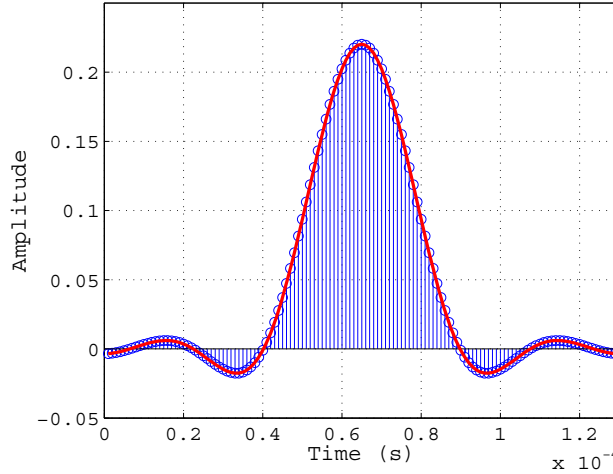


Fig. 9 The root-raised cosine waveform used in our pulse tests. Blue stems indicate digitally generated samples at the transmitter and the red curve the actual waveform output by the DAC for transmission. Pulse duration is 1.28×10^{-4} s.

In our tests, the transmitter location is fixed and the pulse train is continuously emitted. The receiver, mounted on a robot, is navigated to a given point and stopped. Data are then collected for $\frac{1}{8}$ s, after which collection is terminated until the receiver navigates to the next collection point. For each unique receiver position, 125 pulses

are collected, corresponding to the transmitted complex baseband signal:

$$p_T(t) = \sum_{k=1}^{125} p_c(t - kT), \quad (4)$$

where $T = 10^{-3}$ and the receiver samples the passband signal at 100 MSPS, decimates the sampled signal to 25 MSPS, and then digitally mixes the signal to baseband using a local estimate of the carrier frequency. The resulting digital signal at complex baseband is denoted by

$$r(n) = p_T(n) * h(n) + b(n), \quad (5)$$

where $h(n)$ is the channel impulse response, and $b(n)$ is assumed to be an additive white Gaussian noise (AWGN) random process. In the analysis that follows, we assume that the channel is constant for each $\frac{1}{8}$ s collection time, i.e., all 125 pulses see an identical channel.

The received complex baseband pulse train $r(n)$ is passed through a matched filter (MF) whose template is the RRC pulse shape. Denote by p_M the output of match filtering $p_c(n)$ against $p(n)$; note that $p_M(n)$ is a complex valued signal with the n_{th} sample having the same value on both the I and Q channels. We then estimate timing and compute the average of the MF individual pulse responses, given by

$$p_R(n) = \frac{1}{125} \sum_{i=1}^{125} p_{M,i}(n), \quad (6)$$

where $p_{M,i}(n)$ denotes the MF response to the i_{th} received pulse. Given the RRC pulse shape, $p_{M,i}(n)$ is ideally a raised cosine shape if there were no noise or channel distortion. The additive noise effect is minimized by averaging the individual MF responses.

To test for deviation from an ideal channel without multipath, we compute the observed channel transfer function given by

$$H_R = \frac{\mathcal{F}(p_R)}{\mathcal{F}(p_M)}, \quad (7)$$

where \mathcal{F} denotes the discrete Fourier transform (DFT) computed via an fast Fourier transform (FFT) algorithm. Here $\mathcal{F}(p_R)$ is the DFT of the measured averaged received pulse after matched filtering, and $\mathcal{F}(p_M)$ is the DFT of the ideal matched filter response (a raised cosine pulse). Without multipath, the LTI channel consists of scaling and a single delay only, as discussed in Section 2. We normalize the initial delay to zero, and the maximum transfer function amplitude to unity, so that ideally $|H_R| = 1$ with phase equal to zero.

Multipath propagation induces frequency-dependent deviations from the ideal transfer function in both magnitude and phase, so we consider 2 measures of channel distortion. Let S denote the selected set of frequencies under test, taken from the DFT. We define a mean-square error (MSE) of the difference between the measured and ideal unity magnitude response given by

$$M = \frac{1}{|S|} \sum_{f \in S} [|H_R(f)| - 1]^2. \quad (8)$$

The MSE of the difference between the measured channel phase response and its ideal zero value is given by

$$P = \frac{1}{|S|} \sum_{f \in S} [\angle H_R(f)]^2. \quad (9)$$

These 2 measures, sample averages computed across the DFT frequency bin set S , capture the discrepancy of the measured channel H_R from an idealized all-pass, zero-phase filter. Note that for each fixed transmit-receive location, there is a single channel realization H_R , and hence one value for M and one for P for each experimental receiver position.

Recall our decimated sampling rate is 25 MSPS with a pulse bandwidth of 30 kHz, so we are considerably above the Nyquist rate. We use a 1-sided DFT frequency grid of 0 to 50 kHz, with grid spacing $\Delta f \approx 6$ Hz. The set S consists of those frequency values on the grid where the spectrum of the ideal received raised cosine

pulse, $|\mathcal{F}(p_M)|$, exceeds 0.01, where the maximum magnitude has been normalized to 1. Small values for P provide evidence of minimal phase distortion, and small values for M are indicative of a constant attenuation with respect to frequencies probed by the pulse. As described in the next section, in Scenario 3, we employ the robotic platform to repeat the above procedure for hundreds of measurement locations (keeping transmitter location fixed while varying receiver location).

4.2.2 Wider Bandwidth Pulse Tests

The transmit pulse bandwidth can easily be increased or decreased in the SDR transmitter by changing the sampling rate when generating the RRC waveform. In addition to the above case, we also generated an RRC pulse stream with symbol duration of $T_S = 1.935 \times 10^{-6}$ with single pulse duration of 7.74×10^{-6} s. In this case we transmit 10,000 pulses per second, so that the total time between 2 consecutive pulse starts is $T = 10^{-4}$ s. The RRC pulse has 3-dB bandwidth of approximately 500 kHz and a 10-dB bandwidth of 800 kHz. The 1-sided DFT grid over which we evaluate M and P for this case ranges from 0 to 1 MHz. Receiver processing for this case then follows as described above for the narrowband pulse tests.

4.3 Tone Tests

A second phase distortion analysis technique is also pursued, which is based on tones transmitted simultaneously over the air and via a cabled reference channel, shown in Fig. 3b. These tests were conducted by moving the receiver to each new Rx location. Tone frequencies are selected within [39.5, 40.5] MHz. The transmit signal is divided between the antenna and an SMA cable (reference) using a power divider. Likewise at the receiver, complex baseband samples of the 2 separate signals are acquired simultaneously from the 2 channels by using the 2 ports on the BasicRx card, which are controlled by the same clock. For a given frequency, the instantaneous received phase is computed for both the antenna signal and the reference. The difference in instantaneous phase, averaged over all samples collected at a given frequency f , yields our estimate of the phase response at f .

4.4 Bit Error Rate (BER) Measurements

In addition to the above channel sounding tests, BER measurements were carried out at a center frequency of 40 MHz, where the receiver estimates timing and carrier offset, but does not equalize for any delay-spread in the channel. At the transmitter,

packets of length 1000 symbols are generated with random data, quadrature phase shift keying (QPSK)-modulated with Gray coding, and per symbol RRC filtered. We transmit 62,000 QPSK symbols per second, corresponding to a data rate of 120 kbps. A Barker code prefix is also incorporated into each packet to aid synchronization.⁵³

At the receiver, the complex baseband signal is sampled at 1 MSPS. After applying an RRC pulse matched filter, symbol timing is recovered using the early-late gate method.⁵⁴ Next, cross-correlation against the Barker code prefix is used to estimate and correct the frequency offset. Finally, the Barker code is also used to estimate and correct for phase offset and attenuation via a complex scalar multiplication. We emphasize that equalization consists of a single scalar complex multiplication, and no attempt is made to estimate or compensate for any presumed delay spread in the channel. The QPSK BER is estimated over 10^8 bits, and the observed signal-to-noise ratio (SNR) recorded.

5. Experimental Results

5.1 Path Loss

We first report on the path loss observed in Scenario 3. We use the pulse data described in Section 4, for Case 5a in Table 1 (outdoor, NLOS). For each fixed Rx location, raw I and Q samples are collected spanning 125 pulses, which are used to compute an uncalibrated pulse power (P_r^{uncal}). It is uncalibrated because the way the USRP processes data, the I and Q samples do not map linearly to the actual receive power; USRP gain calibration is discussed below. Simultaneously, we also store GPS location information. The GPS data are post-processed and enhanced for accuracy. Such enhancement is accomplished by leveraging the auxiliary sensors of the robot, including IMU, laser scanner, and odometry, to localize the platform with reference to a fixed Universal Transverse Mercator (UTM) origin. We then correct the processed GPS coordinates by introducing a translation offset using measured ground truth and Google Maps as a reference.

To calculate the path loss at a fixed location, the out-of-band noise is reduced with a narrowband bandpass filter. Next, P_r^{uncal} is computed by finding the peak value of $|P_c(n)|^2$ (the “peak power”) for each pulse in the pulse train received at that location, and then averaging across all these peak power values. After the peak power values are calculated, the channel path loss (in dB) is computed using

$$PL = P_t - P_r^{uncal} + G_t + G_r + G_{sys}, \quad (10)$$

where P_t and P_r^{uncal} are the transmit and receive powers in dBm, respectively. Here, G_t and G_r are the gains of the Tx and Rx antennas, and G_{sys} is the sum of all other system gains and losses including amplifier gain, filter loss, and cable losses. G_{sys} also includes a calibration factor for the USRP to map I and Q values to true power levels. This calibration factor was computed by directly connecting the USRP to a signal generator via an radio frequency (RF) cable and performing a power sweep to map the quantity captured by (P_r^{uncal}) to actual signal power in dBm.

Next, the corrected GPS data are used to find the distance between the receiver and transmitter at all measurement points. The range data are binned into intervals of size 0.45λ , with the path-loss data mapped to its corresponding bin, and the mean and standard deviation of all path loss values falling in a given bin are computed. The binning size is experimentally chosen to be similar to the position error of our system. The overall position error attributable to our measurement system is within ± 1.5 m, which comes from errors in the GPS data and SLAM processing. It should be noted that the linear path loss trend does not change when the bin size is reduced, although the path-loss curve will not be as smooth and has a slight increase in standard deviation for the linear fit.

The path-loss mean and standard deviation versus range is shown in Fig. 10, which is based on measurements in Scenario 3 (case 5a) and consists of a total of 152 collection points. The path loss for this case has a standard deviation of 2 dB from the least squares fit. The calculated path-loss exponent is 6.3. This path-loss exponent value is slightly higher than typical indoor/outdoor path-loss exponent values reported in the literature for the upper VHF, UHF, and microwave range (roughly 4 to 6.5).^{55,56} In the lower VHF with low antenna heights ($\leq 0.5\lambda$), propagation is primarily supported by surface waves, resulting in the higher path-loss exponent value because surface waves decay faster in general.^{36,57} Note, however, that while the path-loss exponent is relatively high, the overall attenuation is much less than expected at higher frequencies due to lower penetration loss through the walls.³³ It should also be noted that other measurements in Scenario 3 (with different Tx locations) have resulted in path-loss exponent values ranging from 4 to 5. The path-loss variation depends on the number of obstacles and buildings in the path. Our reported measurements in Scenario 3 are a challenging case with a significant num-

ber of structures in the typical LOS path.

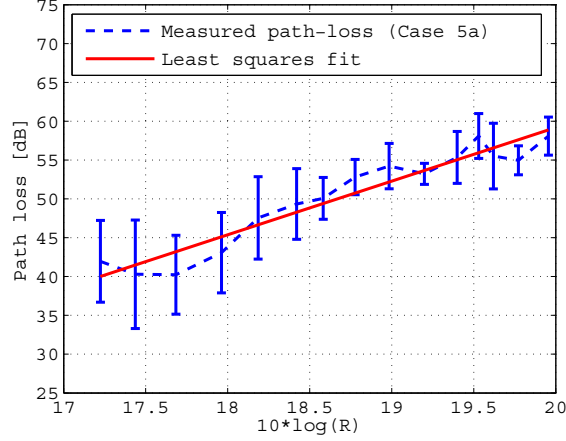


Fig. 10 Mean (dashed line) and standard deviation (solid vertical bars) of measured path loss in Scenario 3 (Fig. 8 Case 5a in Table 1). The solid line is the least squares fit. The path-loss statistic shown is computed using a total of 152 measurement points with over 10,000 measured pulses, where each pulse consists of 3,200 samples.

A more extensive measurement-based path-loss characterization for VHF indoor/outdoor channels, as well as comparison against measurements at 2.4 GHz, is presented in a previous paper.³³ Although the measurements were carried out in different indoor and outdoor scenarios, the path-loss results presented³³ are comparable to the path-loss results discussed in this report.

5.2 Phase Distortion and Instantaneous Phase

Multipath or other propagation effects can generally introduce phase distortion. To look more closely at this, we examine the instantaneous phase for 2 representative pulse cases. In Fig. 11 we plot instantaneous phase against time, for 2 complex baseband pulses from Scenario 3 case 5b, receiver location R_6 (see Table 1 and Fig. 8). The instantaneous phase plotted in Fig. 11 consists of the middle 1250 samples of the received pulse, out of 3200 samples per pulse. Receiver processing consisted of bandpass filtering to reduce out-of-band noise, passband sampling, frequency offset estimation, and mixing to complex baseband. No matched filter processing or averaging was used. The plots represent arbitrarily chosen 60th and 120th pulses of the 125 collected at this particular Rx position, and the SNR was measured to be close to 20 dB for each pulse. In fact, the entire ensemble of 125 pulses all show the same instantaneous phase as in Fig. 11. Note that quadrature results in a constant noise-free pulse phase of $\pi/4$, which has been removed for plotting. Also, carrier

frequency offset error will result in a linear phase change with time; we estimate and remove this linear trend before plotting.

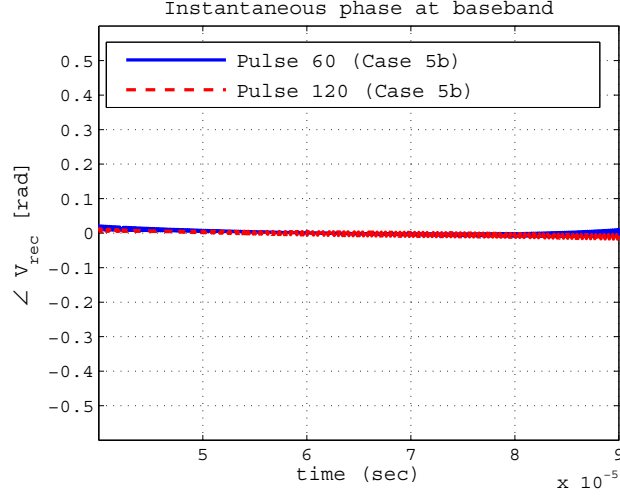


Fig. 11 Instantaneous phase vs. time for 2 example complex baseband received pulses after frequency offset correction, for a receiver position selected from Case 5b (see Fig. 8 and Table 1). Little phase distortion is evident for high SNR cases such as these.

After removing the $\pi/4$ offset and linear trend due to carrier offset, plots of instantaneous phase display remarkably little variation from zero for these and all other high SNR cases examined, demonstrating very little observed phase distortion. The slight variation in the phase plots is well within what can be expected due to the inherent limitations of our measurement system.

5.3 Statistical Analysis of the Measured Channel Transfer Function

Next we report on the measured statistics of the channel transfer function as described in Section 4, using the error measures M and P from Eqs. 8 and 9, respectively (Figs. 12-14). To establish baseline distributions for M and P for each fixed SNR, we simulate a channel that introduces only attenuation and AWGN (an ideal all-pass zero-phase transfer function). We perform the identical transmit and receive data generation and processing that we do in our actual data collection based on processing a pulse train, as described in Section 4. For each SNR value, we conducted 500 Monte Carlo trials over realizations of the additive noise. We used the resulting empirical distributions of M and P to find a lower $1 - \alpha$ confidence interval for each, i.e., we find threshold values τ_M and τ_P such that $\Pr(M > \tau_M) = \alpha$ and $\Pr(P > \tau_P) = \alpha$. Note that these threshold values are a function of the test SNR. For our tests, we use $\alpha = 0.05$ to yield a 95% confidence level.

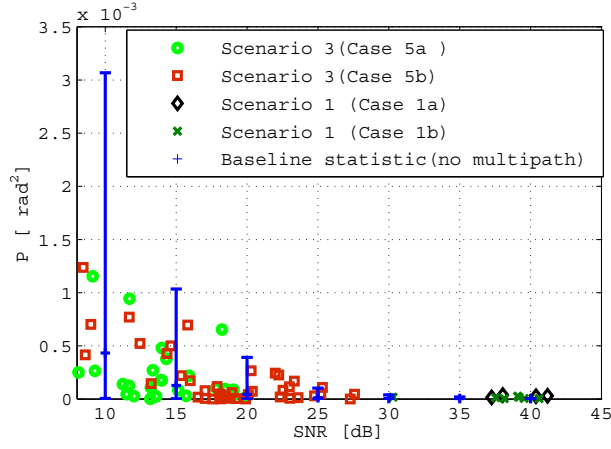


Fig. 12 Mean square deviation of the received signal phase compared with an ideal channel transfer function for cases 5a and 5b (see Fig. 8 and Table 1). P measures deviation from the ideal zero channel transfer function phase. Little statistical deviation is observed at the 95% level.

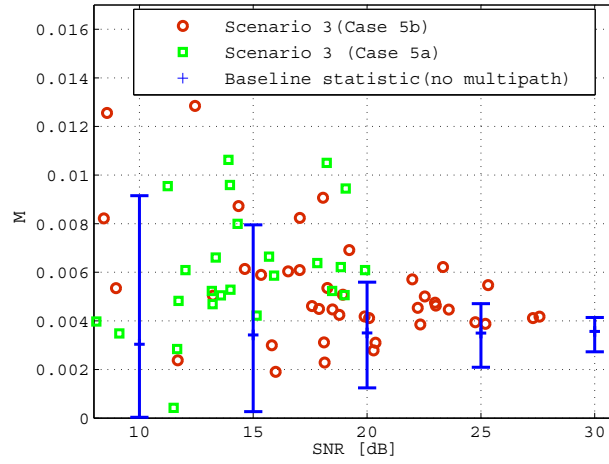


Fig. 13 Mean square deviation of the received signal amplitude compared with an channel transfer function for Cases 5a and 5b (see Fig. 8 and Table 1). M measures deviation from the ideal unity gain transfer function amplitude. Only a small deviation is observed.

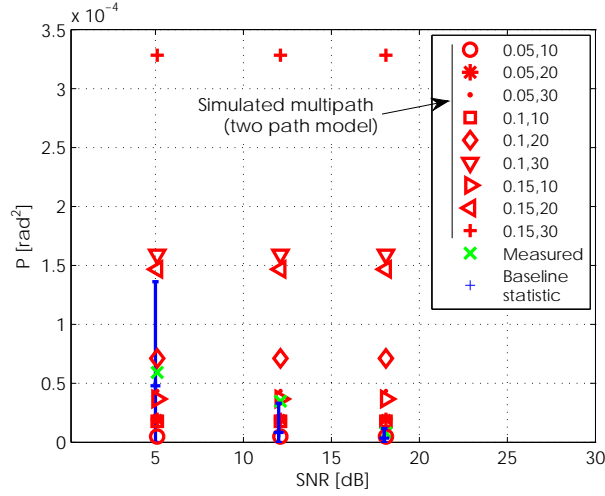


Fig. 14 Mean square deviation of the measured phase for case 3d (see Fig. 8 and Table 1), along with various realizations of theoretical multipath channels based on a 2-path channel model. The first and second numbers in the legends of the theoretical multipath points are the normalized amplitude and delay of the secondary (multipath) component with respect to the dominant component. Note that the dominant component is normalized to have energy 1 and delay 0. A 95% confidence interval for the distribution of the phase statistic under an ideal flat fading channel with AWGN is shown (blue bar). Note that most multipath channels fall outside the blue bar; this shows our test has good statistical power in being able to detect multipath. Also note that actually obtained experimental values (green x) falls within or very near the blue bar.

Figures 12 and 13 depict experimental results for measurements carried out in Scenario 3 and Scenario 1. These results consist of 11 and 97 different Rx positions in Scenario 1 and Scenario 3, respectively. The data collected at each measurement point consists of 250 pulses in the case of Scenario 1 and 125 pulses in the case of Scenario 3 resulting in a total of 14875 measured pulses. For each SNR, the intervals $(0, \tau_M)$ and $(0, \tau_P)$ are also shown as vertical blue bars. Note that in Fig. 13, these bars have a slight upward bias from their ideal lower end point of 0. This is attributable to a small departure from unity gain due to roll-off in the magnitude response of the lowpass filter used in processing the pulses. Statistical evidence of deviation from the ideal transfer function exists at level α if, for a particular computed value, $M > \tau_M$, or $P > \tau_P$.

The phase statistic P in Fig. 12 shows that all the Rx positions considered resulted in a channel transfer function whose phase deviation from an ideal delay and attenuation channel is well within statistical limits caused by additive noise. We cannot reject the ideal transfer function model at the $\alpha = 0.01$ level. The amplitude statistic shown in Fig. 13 shows similar results, with most measurements within the statistical limits, although there is some deviation. However, this statistical deviation is small, and appears to be independent of the phase results. A more refined analysis could consider the joint distribution of M and P , although only a small variation in attenuation is observed, and the transfer function phase seems more pertinent to the measurement of phase distortion.

The phase and amplitude statistics are also computed for the wideband pulse tests described in Section 4. Figure 14 shows the phase statistic calculated based on measurements carried out in Scenario 2 where a few LOS and NLOS points were measured. Similar to the previous case, the phase deviation in 2 of the 3 cases falls within the 95% confidence intervals of the null hypothesis; the third is just slightly outside it. In this figure, we also show the theoretical phase MSE for various 2-component multipath channels, i.e., channels consisting of a dominant component and a single multipath component. We show channels whose secondary component has energy which is a fraction α of the dominant signal, and delay of γ meters relative to the dominant signal, for various values of α and γ (as shown in the figure legend). For example, the point $\alpha = 0.05$, $\gamma = 10$ represents the phase deviation statistic value we would obtain for a 2-component multipath channel, whose secondary component is 0.05 as strong as the primary one, and which travels an excess distance (in free space) of 10 m. Note that for the higher SNR cases,

most multipath channels give phase MSE values that fall outside the null hypothesis interval; this indicates that the test has strong statistical power. Also, note that in general, as the secondary component's relative energy and/or delay increases, the value of the statistic grows. This shows that our statistic P has the desirable property that it grows larger as the multipath becomes worse in amplitude and delay. Finally, note that the various multipath channel statistics are point estimates computed in the absence of AWGN. Had we also introduced AWGN, the points would become intervals and would shift strictly up, as AWGN increases phase MSE. We have not shown these latter intervals, so as not to clutter the figure.

The amplitude statistic shows qualitatively similar results; however, the Tx and Rx antennas exhibit small amplitude variations (i.e., are not constant gain) over the pulse bandwidth, which affects our magnitude MSE statistic. Note that this is more of an issue for the wider bandwidth pulses than the narrow bandwidth pulses, as the larger bandwidth results in a larger overall deviation from constant gain. The net effect of this system non-ideality is to add noise to our magnitude MSE statistic. Rather than carefully compensate for the effect of this antenna gain variation on our magnitude statistic, we have focused on the phase statistic.

5.4 Tone Tests for Transfer Function Phase Measurement

Next we present results for tone tests as described in Section 4.2.2, where we measure the phase difference between the received tone via the antenna and via the cabled reference channel. Experimental results are plotted in Figs. 15, 16, and 17, with the specific cases listed in the captions of each figure. The curves show the results for NLOS cases collected in Scenario 1, shown in Fig. 6. At each measurement location, we collect 2×10^6 (I,Q) samples from the 2 channels for each frequency. With the sampling rate of 2 Ms/s, this corresponds to a 1-s collection time. The phase difference is calculated for each sample, and the mean and standard deviation of the phase difference is plotted.

The experimental results show a strong linear phase relationship as a function of frequency for the entire range of test tones in [39.5, 40.5] MHz. Some deviation is expected due to varying SNR and other experimental effects, but the measured deviation is small as shown in the figures (note the vertical scale is in radians). This approach is a direct way of measuring the presence or absence of phase distortion, since phase deviation is measured with respect to the low distortion cable reference channel. The observed low-deviation linear phase as a function of frequency con-

firmly that the channel largely consists of a single dominant propagation path for all cases tested.

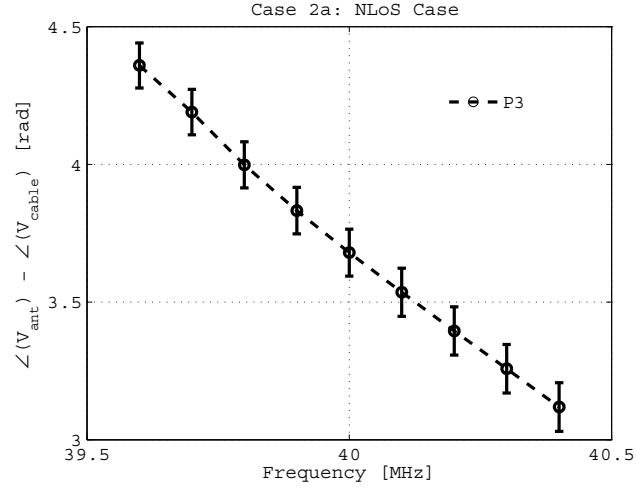


Fig. 15 Tone tests: Mean and standard deviation of the measured phase difference between the wireless and reference channels for Case 2a, at Rx point P3 (see Fig. 6 and Table 1)

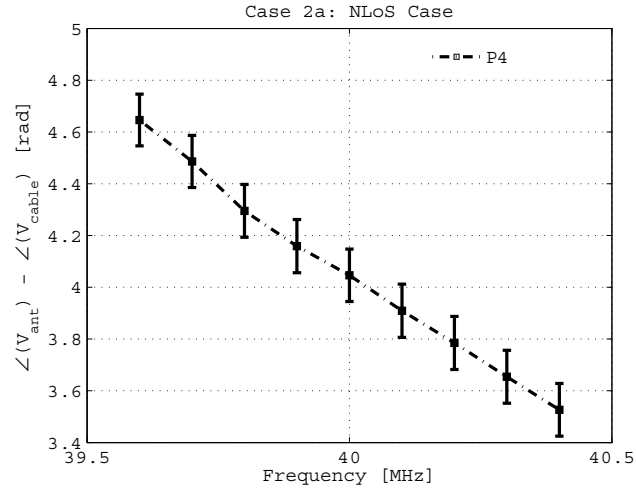


Fig. 16 Tone tests: Mean and standard deviation of the measured phase difference between the wireless and reference channels for Case 2a, at Rx point P4 (see Fig. 6 and Table 1)

We note that phase and amplitude distortion will occur as the frequency increases, an effect that will become evident within the VHF band. In a previous publication, the authors investigated the propagation characteristics at HF/lower VHF as compared to 100 MHz and higher, using full-wave simulations.³ For a given indoor building scenario, the effect of multipath and channel induced distortion is clearly evident at 100 MHz, but is very minimal at lower frequencies such as 20 or 40

MHz. This is easily seen in the signal (both amplitude and phase) coverage inside the building.³ A single tone test, when carried out at several different locations in a relatively confined environment, will show evidence of multipath in both amplitude and phase, if such multipath is present.

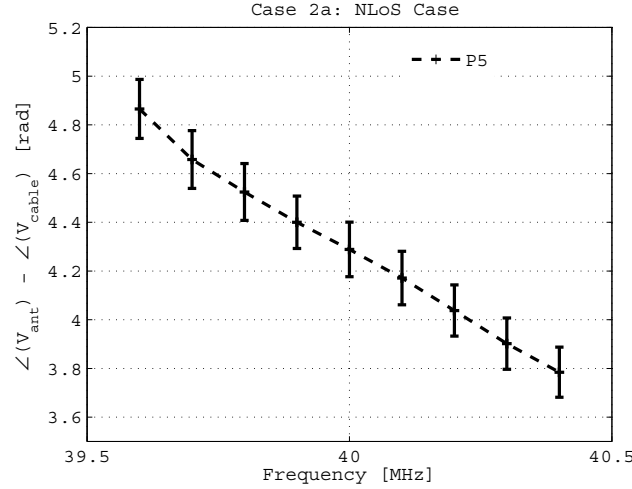


Fig. 17 Tone tests: Mean and standard deviation of the measured phase difference between the wireless and reference channels for Case 2a at Rx point P5 (see Fig. 6 and Table 1)

5.5 BER Measurement Results

Finally, we report on BER tests, as described in Section 4.2.2. These tests were carried out in Scenario 2, with the Tx location fixed and the Rx position varied as shown in Fig. 7, yielding both LOS and NLOS cases. Figs. 18 and 19 show the measured BER vs. SNR curves for the LOS and NLOS scenarios, respectively. Also plotted is a theoretical QPSK BER for an AWGN channel. The measured SNR was estimated for each Rx position (generally declining as range was increased). We see excellent agreement between theoretical and measured BER, with some small deviations attributable to finite size effects arising from the number of bits collected. As noted in Section 4.2.2, the receiver processing only corrected for carrier frequency offset and phase correction, and did not attempt to correct for any delay spread. Unlike at higher frequencies such as higher VHF, UHF, and microwave, the observed lower VHF channel in a dense indoor scene with large metal obstacles behaved as an ideal AWGN channel, such that ideal BER results were obtained with very simple receiver processing.

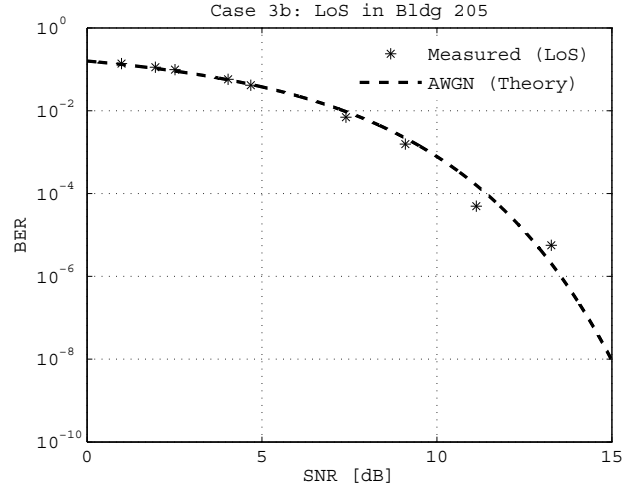


Fig. 18 Theoretical and measured BER vs. SNR curves for LOS indoor channel Scenario 2 (Case 3b, See Table 1 and Fig. 7). Simple receiver processing achieves the theoretical performance limit predicted for an AWGN channel.

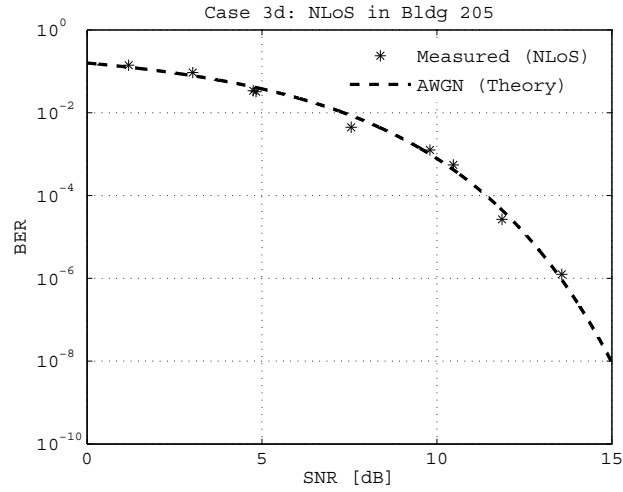


Fig. 19 Theoretical and measured BER vs. SNR curves for NLOS indoor channel Scenario 2 (Case 3d, See Table 1 and Fig. 7). The theoretical performance limit is attained in this NLOS case.

6. Conclusion

In this report, we have characterized the lower VHF band wireless channel around 40 MHz in highly cluttered environments using an extensive measurement campaign including statistical analysis of thousands of transmissions. Our objective was to study the viability of low power, short-range, reliable communications that are minimally affected by the presence of clutter, and establish the degree to which phase distortion is present or absent as is relevant to geolocation in these environments.

FDTD electromagnetic simulations of an indoor/outdoor scene showed little phase distortion or multipath propagation that is so characteristic of upper VHF and above. This helped motivate our study of phase distortion, channel transfer function, and communications BER. Tone and pulse-based measurements were conducted in 3 different scenarios, primarily in NLOS cases, over ranges of 10 to 200 m. Using SDRs for both transmit and receive, and integrating the receiver onto a robotic platform, gave us experimental flexibility to collect tens of thousands of measurements.

Shorter-range measurements carried out inside 2 different buildings (Scenarios 1 and 2), as well as medium-range measurements performed in a complex indoor/outdoor propagation environment (Scenario 3) were used to quantitatively study path loss, phase distortion, and channel transfer function. It was shown that the channel phase distortion is minimal both in LOS and NLOS scenarios, even when several layers of obstacles are present between the Tx and Rx nodes. The channel phase distortion was analyzed using 2 independent techniques, including tone tests that incorporated a cable reference channel for precise phase comparisons.

Pulse tests were used to estimate the empirical channel transfer function in [39.5, 40.5] MHz, and we found no statistical evidence against a simple scalar attenuation and AWGN channel model. We performed tone tests by which the ideally expected linear variation of phase as a function of frequency was confirmed. We also showed that BER measurements carried out in the same environments show very good agreement with the theoretically predicted AWGN channel BER curve, for both LOS and NLOS cases.

Thus, our central finding is that for low power, short-range low data rate communications in cluttered environments, the lower VHF channel can be modeled as an AWGN channel with scalar attenuation. The simplicity of the channel, along with

recent advances in the design of extremely miniaturized lower VHF antennas, can be exploited in a large variety of signal processing and communications applications including geolocation in GPS-denied environments and voice communications in search-and-rescue operations.

7. References

1. Hampton JR, Merheb N, Lain W, Paunil D, Shuford R, Kasch W. Urban propagation measurements for ground based communication in the military uhf band. *Antennas and Propagation, IEEE Transactions on*. 2006;54(2):644-654.
2. Andrusenko J, Miller R, Abrahamson J, Merheb Emanuelli N, Pattay R, Shuford R. Vhf general urban path loss model for short range ground-to-ground communications. *Antennas and Propagation, IEEE Transactions on*. 2008;56(10):3302-3310.
3. Dagefu F, Oh J, Sarabandi K. A sub-wavelength rf source tracking system for gps-denied environments. *Antennas and Propagation, IEEE Transactions on*. 2013;61(4):2252-2262.
4. Dagefu F, Oh J, Choi J, Sarabandi K. Measurements and physics-based analysis of co-located antenna pattern diversity system. *Antennas and Propagation, IEEE Transactions on*. 2013;61(11):5724-5734.
5. Barnett W. Multipath propagation at 4, 6, and 11 ghz. *Bell System Technical Journal, The*. 1972;51(2):321-361.
6. Ruthroff C. Multiple-path fading on line-of-sight microwave radio systems as a function of path length and frequency. *Bell System Technical Journal, The*. 1971;50(7):2375-2398.
7. Ali-Rantala P, Ukkonen L, Sydanheimo L, Keskilammi M, Kivikoski M. Different kinds of walls and their effect on the attenuation of radiowaves indoors. In: *Antennas and Propagation Society International Symposium, 2003. IEEE; Vol. 3; p. 1020–1023 vol.3*.
8. Raleigh G, Cioffi J. Spatio-temporal coding for wireless communication. *Communications, IEEE Transactions on*. 1998;46(3):357-366.
9. Sadler B, Swami A. On the performance of episodic uwb and direct-sequence communication systems. *Wireless Communications, IEEE Transactions on*. 2004;3(6):2246-2255.
10. Tarokh V, Jafarkhani H, Calderbank A. Space-time block codes from orthogonal designs. *Information Theory, IEEE Transactions on*. 1999;45(5):1456-1467.

11. Rigling B. Urban rf multipath mitigation. *Radar, Sonar Navigation, IET*. 2008;2(6):419-425.
12. Zhang Z, Law C. Short-delay multipath mitigation technique based on virtual multipath. *Antennas and Wireless Propagation Letters, IEEE*. 2005;4:344-348.
13. Closas P, Fernández-Prades C, Fernández-Rubio J. A bayesian approach to multipath mitigation in gnss receivers. *Selected Topics in Signal Processing, IEEE Journal of*. 2009;3(4):695-706.
14. Alvarez Y, Las-Heras F, Pino M. Full-wave method for rf sources location. In: *Antennas and Propagation, 2007. EuCAP 2007. The Second European Conference on*; p. 1–5.
15. Oh J, Choi J, Dagefu F, Sarabandi K. Extremely small two-element monopole antenna for hf band applications. *Antennas and Propagation, IEEE Transactions on*. 2013;61(6):2991-2999.
16. Oh J, Sarabandi K. A moderate gain extremely short hf monopole antenna. In: *Antennas and Propagation (EUCAP), 2012 6th European Conference on*; p. 1657–1660.
17. Frequency allocation table. [date unknown; accessed 2015 Mar]. <http://transition.fcc.gov/oet/spectrum/table/fcctable.pdf>.
18. Single channel ground and airborne radio system (sincgars). [date unknown; accessed 2015 Mar]. <http://en.wikipedia.org/wiki/SINCGARS>.
19. Wyne S, Singh A, Tufvesson F, Molisch A. A statistical model for indoor office wireless sensor channels. *Wireless Communications, IEEE Transactions on*. 2009;8(8):4154-4164.
20. Kaya A, Greenstein L, Trappe W. Characterizing indoor wireless channels via ray tracing combined with stochastic modeling. *Wireless Communications, IEEE Transactions on*. 2009;8(8):4165-4175.
21. Wallace J, Jensen M. Modeling the indoor mimo wireless channel. *Antennas and Propagation, IEEE Transactions on*. 2002;50(5):591-599.
22. Nerguizian C, Despins C, Affes S, Djadel M. Radio-channel characterization of an underground mine at 2.4 ghz. *Wireless Communications, IEEE Transactions on*. 2005;4(5):2441-2453.

23. Rappaport T. Characterization of uhf multipath radio channels in factory buildings. *Antennas and Propagation, IEEE Transactions on*. 1989;37(8):1058-1069.
24. Lecours M, Delisle GY, Chouinard JY, Ahern J. Envelope, phase and data-transmission characterization for mobile radio channels at uhf frequencies. *Electrical and Computer Engineering, Canadian Journal of*. 1992;17(4):175-182.
25. Perez-Vega C, Zamanillo J. Path-loss model for broadcasting applications and outdoor communication systems in the vhf and uhf bands. *Broadcasting, IEEE Transactions on*. 2002;48(2):91-96.
26. Rowe G, Williamson A, Egan B. Mobile radio propagation in auckland at 76 MHz. *Electronics Letters*. 1983;19(25):1064-1065.
27. Paolini E. Attenuation measurements of mf, hf, and vhf waves over the ground surface. *Electromagnetic Compatibility, IEEE Transactions on*. 1968;EMC-10(3):307-312.
28. Pugh JA, Bultitude R, Vigneron PJ. Path loss measurements with low antennas for segmented wideband communications at vhf. In: *Military Communications Conference, 2006. MILCOM 2006. IEEE*; p. 1–5.
29. Pugh JA, Bultitude R, Vigneron PJ. Propagation measurements and modelling for multiband communications on tactical vhf channels. In: *Military Communications Conference, 2007. MILCOM 2007. IEEE*; p. 1–7.
30. Vigneron P, Pugh J. Propagation models for mobile terrestrial vhf communications. In: *Military Communications Conference, 2008. MILCOM 2008. IEEE*; p. 1–7.
31. Okumura Y, Ohmori E, Kawano T, Fukuda K. Field strength and its variability in vhf and uhf land-mobile radio service. *Rev. Elec. Commun. Lab*. 1968;16(9):825–73.
32. Hatay M. Empirical formula for propagation loss in land mobile radio services. *Vehicular Technology, IEEE Transactions on*. 1980;29(3):317–325.
33. Dagefu F, J C, M S, B S, K S. Performance assessment of lower vhf band for short range communication and geolocation applications. *Radio Science*. 2015;50:1-10.

34. Kurner T, Cichon DJ, Wiesbeck W. Evaluation and verification of the vhf/uhf propagation channel based on a 3-d-wave propagation model. *Antennas and Propagation, IEEE Transactions on*. 1996;44(3):393–404.
35. Thiel M, Sarabandi K. 3d-wave propagation analysis of indoor wireless channels utilizing hybrid methods. *Antennas and Propagation, IEEE Transactions on*. 2009;57(5):1539–1546.
36. Dagefu F, Sarabandi K. Analysis and modeling of near-ground wave propagation in the presence of building walls. *Antennas and Propagation, IEEE Transactions on*. 2011;59(6):2368–2378.
37. Sarabandi K, Koh IS. Effect of canopy-air interface roughness on hf-vhf wave propagation in forest. *Antennas and Propagation, IEEE Transactions on*. 2002;50(2):111–121.
38. Sarabandi K, Koh IS. A complete physics-based channel parameter simulation for wave propagation in a forest environment. *Antennas and Propagation, IEEE Transactions on*. 2001;49(2):260–271.
39. Li Y, Wu MF, Yilmaz AE, Ling H. Investigation of short-range radiowave propagation at hf/vhf frequencies in a forested environment. *Antennas and Wireless Propagation Letters, IEEE*. 2009;8:1182–1185.
40. Meng YS, Lee YH, Ng BC. Wideband channel characterization in a tropical forested area. In: *Microwave Conference, 2007. APMC 2007. Asia-Pacific*; p. 1–4.
41. Warnick KF, Gottula RB, Shrestha S, Smith J. Optimizing power transfer efficiency and bandwidth for near field communication systems. *Antennas and Propagation, IEEE Transactions on*. 2013;61(2):927–933.
42. Schälfert T, Vossiek M. Transponder and reader concept for a hf locating system. In: *Microwave Conference (GeMIC), 2011 German*; p. 1–4.
43. Gunashekar S, Warrington E, Salousf W, Bertel L, Lemur D, Zhang H, Abbasi N. An experimental investigation into the feasibility of mimo techniques within the hf band. In: *Antennas and Propagation, 2007. EuCAP 2007. The Second European Conference on*; p. 1–5.

44. Watterson C, Juroshek J, Bensema WD. Experimental confirmation of an hf channel model. *Communication Technology, IEEE Transactions on*. 1970;18(6):792–803.
45. Emag technologies inc.. [date unknown; accessed 2015 Mar]. <http://www.Emagware.com>.
46. Ettus research. [date unknown; accessed 2015 Mar]. <https://www.ettus.com/product/details/UN210-KIT>.
47. Ros. [date unknown; accessed 2015 Mar]. <http://www.ros.org/>.
48. Fink J, Twigg J, Yu P, Sadler B. A parsimonious model for wireless connectivity in robotic networks. In: *Global Conference on Signal and Information Processing (GlobalSIP)*, 2013 IEEE; p. 855–858.
49. Twigg J, Fink J, Yu P, Sadler B. Rss gradient-assisted frontier exploration and radio source localization. In: *Robotics and Automation (ICRA)*, 2012 IEEE International Conference on; p. 889–895.
50. Gnu radio. [date unknown; accessed 2015 Mar]. <http://www.gnuradio.org/>.
51. Verma G, Yu P. A matlab library for rapid prototyping of wireless communications algorithms with the universal software radio peripheral (usrp) radio family. DTIC Document; 2013. Report No.: ARL-TR-6491.
52. Proakis JG. *Digital communications*. McGraw-Hill, New York; 1995.
53. Wyglinski AM, Pu D. *Digital communication systems engineering with software-defined radio*. Artech House, London; 2013.
54. Sklar B. *Digital communications fundamentals and applications*. Prentice Hall, New Jersey; 2001.
55. Zhang X, Burress TW, Albers KB, Kuhn WB. Propagation comparisons at vhf and uhf frequencies. In: *Radio and Wireless Symposium, 2009. RWS'09. IEEE*; p. 244–247.
56. De Toledo AF, Turkmani AM, Parsons J. Estimating coverage of radio transmission into and within buildings at 900, 1800, and 2300 MHz. *Personal Communications, IEEE*. 1998;5(2):40–47.

57. Liao D, Sarabandi K. Near-earth wave propagation characteristics of electric dipole in presence of vegetation or snow layer. *Antennas and Propagation, IEEE Transactions on*. 2005;53(11):3747–3756.

List of Symbols, Abbreviations, and Acronyms

| | |
|----------|---|
| P | pressure |
| ADC | analog-to-digital convertor |
| AWGN | additive white gaussian noise |
| BER | bit error rate |
| DAC | digital-to-analog converter |
| FDTD | finite-difference time-domain |
| GNU | GNU's Not Unix |
| GPS | global positioning system |
| HF | high frequency |
| LOS | line-of-sight |
| MF | matched filter |
| MUL | MATLAB-USRP-Library |
| NLOS | non-line-of-sight |
| QPSK | quadrature phase shift keying |
| ROS | robot operating system |
| SDR | software-defined radio |
| SINCGARS | Single Channel Ground and Airborne Radio System |
| SLAM | simultaneous localization and mapping |
| SSD | solid-state drive |
| UHF | ultra high frequency |
| USRP | Universal Software Radio |
| VHF | very high frequency |

INTENTIONALLY LEFT BLANK.

1 DEFENSE TECHNICAL
(PDF) INFORMATION CTR
DTIC OCA

2 DIRECTOR
(PDF) US ARMY RESEARCH LAB
RDRL CIO LL
IMAL HRA MAIL & RECORDS MGMT

1 GOVT PRINTG OFC
(PDF) A MALHOTRA

8 US ARMY RESEARCH LABORATORY
(PDF) RDRL-CIN-T
F DAGEFU
G VERMA
C RAO
P YU
J FINK
B SADLER
B RIVERA
A KOTT